

## RESEARCH ARTICLE

10.1002/2015JC011362

## Key Points:

- Captured soliton trains in the NE South China Sea using seismic reflection technique
- Extracting waveform and propagation parameters of solitons from seismic data
- Consistency with conventional satellite observation and analytical prediction

## Correspondence to:

Q. Tang,  
tqsh@scsio.ac.cn

## Citation:

Tang, Q., R. Hobbs, D. Wang, L. Sun, C. Zheng, J. Li, and C. Dong (2015), Marine seismic observation of internal solitary wave packets in the northeast South China Sea, *J. Geophys. Res. Oceans*, 120, 8487–8503, doi:10.1002/2015JC011362.

Received 1 OCT 2015

Accepted 2 DEC 2015

Accepted article online 9 DEC 2015

Published online 30 DEC 2015

## Marine seismic observation of internal solitary wave packets in the northeast South China Sea

Qunshu Tang<sup>1,2</sup>, Richard Hobbs<sup>2</sup>, Dongxiao Wang<sup>3</sup>, Longtao Sun<sup>1</sup>, Chan Zheng<sup>4</sup>, Jiabiao Li<sup>5</sup>, and Chongzhi Dong<sup>5</sup>

<sup>1</sup>Key Laboratory of Marginal Sea Geology, South China Sea Institute of Oceanology, Chinese Academy of Sciences, Guangzhou, China, <sup>2</sup>Department of Earth Sciences, Durham University, Durham, UK, <sup>3</sup>State Key Laboratory of Tropical Oceanography, South China Sea Institute of Oceanology, Chinese Academy of Sciences, Guangzhou, China, <sup>4</sup>College of Mathematics and Informatics, South China Agricultural University, Guangzhou, China, <sup>5</sup>Key Laboratory of Submarine Geosciences, Second Institute of Oceanography, Hangzhou, China

**Abstract** Recently the novel seismic oceanography method has been reported to be an effective way to study the energetic internal solitary waves (ISWs) in the northern South China Sea. An optimized seismic-oceanographic cruise was carried out to observe such near-surface ISWs on Dongsha Plateau in July 2014. Several soliton trains rather than single solitons were captured using the seismic technique. After seismic data processing, one prototypical rank-ordered ISW packet on northeast side of Dongsha Island was clearly identified for further analysis. This included waveforms, propagation velocities, and vertical velocities for individual solitons. In this study, an improved scheme was applied to derive the transient phase velocities from the seismic data which is verified from independent satellite and hydrographic data. Analytical predictions from Korteweg-de Vries equation fit better than the extended Korteweg-de Vries equation ignoring background currents. Our results show that the seismic method can be successfully used to image targets in shallow water below 40 m and that seismic oceanography is a promising technique for studying near-surface phenomena with high spatial resolution.

### 1. Introduction

Although the nonlinear internal solitary waves (ISWs, solitons) are ubiquitous in the ocean [Helfrich and Melville, 2006], the northeastern South China Sea (SCS, Figure 1) is arguably the world's best place to study the large amplitude ISWs [e.g., Ramp *et al.*, 2004; Helfrich and Melville, 2006; Buijsman *et al.*, 2010; Vlasenko *et al.*, 2012; Guo and Chen, 2014]. The ISWs are usually formed at Luzon Strait caused by the interaction between the strong tidal currents and the abrupt topography, although the mechanisms, e.g., internal tide steeping and lee-wave formation, are still controversial [e.g., Cai *et al.*, 2002; Yuan *et al.*, 2006; Farmer *et al.*, 2009; Buijsman *et al.*, 2010]. The generated ISWs propagate westward and evolve significantly as they cross the deep basin, steep continental shelf, and shoaling plateau zone, ultimately dissipating on the shallow continental shelf [Guo and Chen, 2014]. These large amplitude and long crest ISWs induce strong under-water currents which have substantial but not well-studied effects on ocean mixing, biological processes, sediments re-suspension, offshore oil engineering, and submarine navigation [Apel *et al.*, 2007; Ramp *et al.*, 2010; Cai *et al.*, 2012], as well as the seismic operation as shown in this study.

Extensive studies have been carried out to study the ISWs using various methods, which can be categorized into three dominant areas: in situ hydrographic observation, satellite remote sensing, and numerical modeling [e.g., Liu *et al.*, 1998; Cai *et al.*, 2002; Ramp *et al.*, 2004]. Echo sounder records using the high-frequency (>10 kHz) backscattered energy can be used to indirectly map internal waves [Farmer and Armi, 1999; Orr and Mignerey, 2003; Klymak and Gregg, 2004; Reeder *et al.*, 2011]; however, finite investigation depth and difficulty in extracting quantitative information has limited the use of these data. Recently, the conventional marine multichannel seismic reflection method with relatively low frequency (5–100 Hz) has been used for ISW observation [Tang *et al.*, 2014b].

Seismic oceanography (SO) [Holbrook *et al.*, 2003] is a rapidly developing area in the study of ocean phenomena based on work by Gonella and Michon [1988] and Phillips and Dean [1991]. The method offers the possibility to

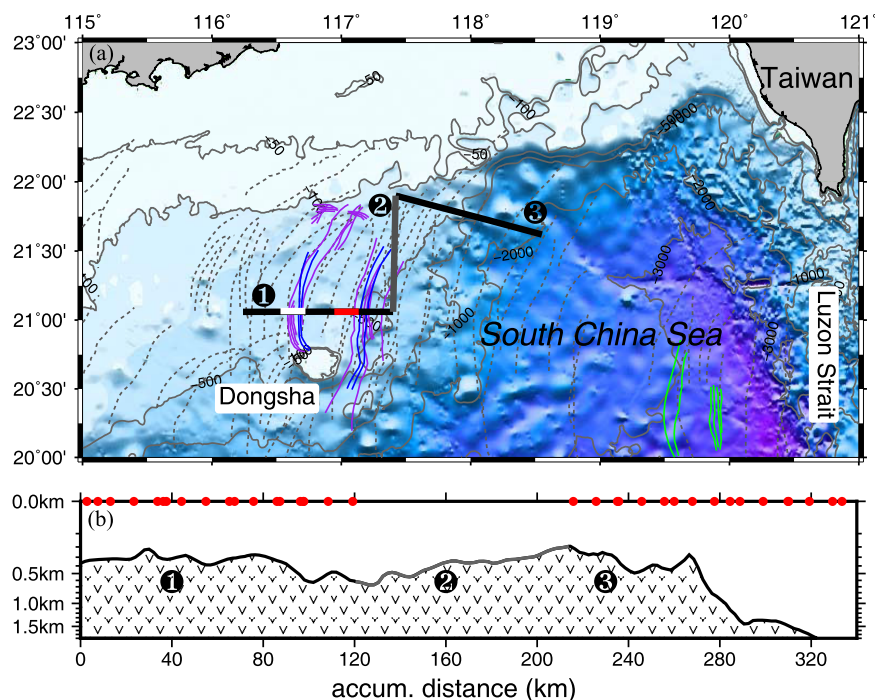


**Figure 1.** (a) Bathymetry map of the NE South China Sea. Thick lines are the seismic lines of the cruise in July 2014. Line 1 (black) consists of a single trip (13 July) and a round trip (27 July). Line 3 (black) is a round trip and Line 2 (gray) is a single trip on 13–14 July. SO1E (red) and SO1E (white) are the subsections on Line 1 where ISW packets were captured on 13 and 27 July, respectively (Figure 6). Gray dashed curves are the surface spread of satellite-imagined ISWs modified from Zhao *et al.* [2004]. The purple and blue curves are the ISW crests from satellite image on the same days with seismic survey on 13 and 27 July, respectively. The green lines in the deep basin show an ISW packet captured on 12 July (Figure 7). (b) Bathymetry along the seismic section. Red dots are the in situ XBT casts.

continuously map thermohaline structure to the full depth of the water column on a vessel steaming at  $\sim 5$  knots. The frequency characteristic of seismic source and the geometry of the seismic streamer give vertical and horizontal resolutions of about 10 m and it is used to observe variety of ocean phenomena including internal waves, eddies, currents, thermohaline staircases, and turbulence, from mesoscale to finescale in the various global ocean environments [e.g., Nakamura *et al.*, 2006; Biescas *et al.*, 2008, 2010; Fer *et al.*, 2010; Pinheiro *et al.*, 2010; Sheen *et al.*, 2011; Buffett *et al.*, 2013; Holbrook *et al.*, 2013; Tang *et al.*, 2013, 2014a]. However, the conventional geometry used for seismic surveying the seafloor makes it difficult to image the near-surface thermohaline structures typically above 200 m because of the minimum offset between the source and receiver array and significant interference from the high-amplitude direct waves [Carniel *et al.*, 2012; Pi  t   *et al.*, 2013; Tang *et al.*, 2014b].

A previous study [Tang *et al.*, 2014b] used the seismic method to detect the ISWs. Monographic and kinematics parameters were derived from the seismic data corroborated with synchronized satellite observations and analytical prediction from in situ hydrographic observation. To further study the ISWs on Dongsha Plateau (Figure 1), a second joint seismic and hydrographic observation was carried out in July 2014. Based on the previous experience, we optimized the survey lines, increased the source energy, and improved the data processing techniques. In summary, at least seven packets of ISWs at different stages of evolution were observed including diffraction, polarity conversion, and disintegration.

In this paper, two typical internal wave packets are presented from different locations. A rank-ordered ISW packet with five well-developed solitons is analyzed for their waveforms, phase velocities, vertical velocities, from the combination of seismic, satellite, and in situ hydrographic data.

## 2. Data and Methods

### 2.1. Seismic Data Acquisition

In July 2014, a seismic cruise was carried out aboard the R/V SHIYAN2 with a primary purpose of capturing ISWs on Dongsha Plateau (Figure 1). Two of the survey lines (Lines 1 and 3) were designed to optimally

image westward propagating ISWs from their generation site in the central Luzon Strait. Vessel headings are orientated normal to the expected wavefronts of ISWs (Figure 1) rather than crossing them obliquely [Tang *et al.*, 2014b, Figure 1]. This arrangement would minimize errors on the parameter estimation as the lines can be assumed to be perpendicular to the wavefronts even if we have no synchronized satellite images to directly measure the wave directions. Line 2 connects Lines 1 and 3 and is orientated in a north-south direction. The total length of the survey lines is  $\sim 600$  km.

There are three important factors that need consideration to ensure that the near-surface structures are captured. First, the characteristics of the seismic source: here we used a source array composed of two Sercel GI guns fired at 2000 psi in harmonic mode with matched generator/injector chamber sizes of 105 cu. in. This configuration was chosen because of its good performance in suppressing bubble oscillation, as this coda is a significant problem for the recovery of the near-surface signals. Second, the near offset (source-receiver distance) was adjusted to reduce the blank zone at the top of the section. We used a 90 m offset which meant we could image structures below  $\sim 40$  m. Third, in order to increase the fold of cover and thus the signal-to-noise ratio (SNR), a shot interval of 25 m was used. The seismic source was towed at 5 m depth so that useful frequencies up to the ghost notch at 150 Hz would be generated. A Sercel Seal oil filled streamer with 120 channels (1500 m length, 12.5 m spacing) was also towed at 5 m depth.

## 2.2. Seismic Data Processing

A representative processing flow for generating the seismic image is (1) defining geometry; (2) noise attenuation; (3) common midpoint (CMP) sorting and velocity analysis; (4) normal moveout (NMO) and stacking. Specific details of these steps are presented below.

1. Defining geometry setting: the geometry was referenced to a UTM Cartesian grid using the shot location data and field acquisition parameters to create the coordinates for the multichannel seismic data.
2. Noise attenuation: the main purpose is to enhance the SNR. Three steps were carried out including (1) bad trace removal, traces with poor SNR were removed; (2) band-pass filtering using a zero-phase 15–120 Hz filter; and (3) direct wave attenuation using an eigenvector filter.

The direct waves, propagating from the source to the receivers, provide the strongest contamination to the near-surface reflection. Therefore, the third step is of particular importance in this study because the signals from the ISWs are extremely close to or overlapping with the direct waves. We used an eigenvector filter to suppress the direct waves based on the Karhunen-Loeve transform [Jones and Levy, 1987]. In practice, if the seafloor is shallow, as in this study, it is necessary to mute the seafloor reflection in the shot gathers to avoid filter noise being generated off the high-amplitude seabed reflection contaminating the data in the water layer. The eigenvector filter was applied on shot gathers after linear moveout using a reduction velocity of 1540 m/s, which was the acoustic velocity close to the surface, which ensured the direct wave arrived at the same time on all offsets. After filtering the reverse linear moveout was used to correct the gathers back into normal. Figure 2 shows an example of a shot gather before and after the eigenvector filter. We can see that the direct waves and associated bubble pulses from the seismic source were significantly attenuated.

3. Seismic data were sorted from shot gathers into CMP gathers. Because the stacking fold (30) was low especially near the surface, the super-gathers from four neighboring CMP gathers were combined for velocity analysis (Figures 3a and 3b).
4. NMO was applied to compensate for offset-dependent moveout so as to make sure the reflections within each CMP gathers were flat (Figure 3c) prior to stacking and generation of the stacked seismic section.

After the above four steps, normally migration would be used to enhance the image quality and correct the position of steep reflectors. We do not use migration for two reasons. First, to keep the water reflections from contamination by migration noise generated from the seafloor. Second, as the water reflections are nearly horizontal so migration would have little effect, even for the steepest ISW the maximum dip angle correction is less than  $0.8^\circ$ . Instead, we applied a mixing step with five channels ( $\sim 30$  m) and an FX deconvolution to attenuate random noise to help increase the SNR.

## 2.3. Velocities From Seismic Data

Because of the redundancy of the multichannel seismic acquisition, we have tens of seismic traces at one CMP position over a finite time span. For the moving waters, this can be used to derive the transient

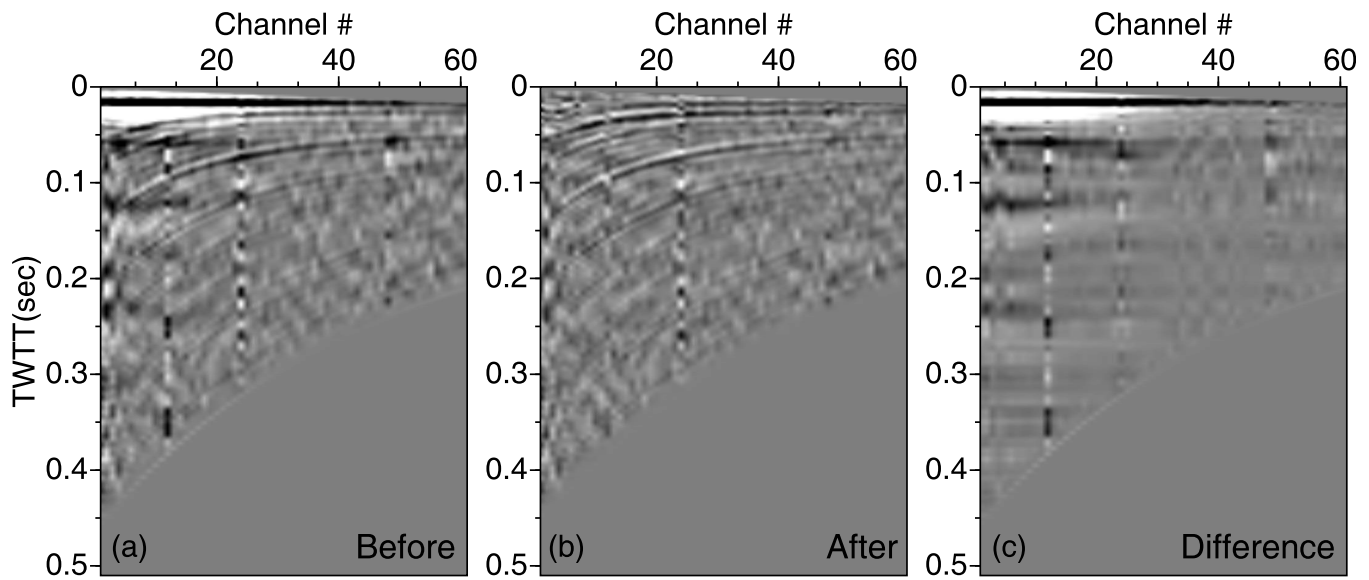


**Figure 2.** An example shows the performance of an eigenvector filter in direct wave attenuation on shot gathers with linear moveout of 1540 m/s applied: (a) before filter, (b) after filter, and (c) their difference. The horizontal and upwardly curved components are the direct waves and the seawater reflections, respectively.

velocities of internal waves from the prestack seismic data [Klaeschen *et al.*, 2009; Vsemirnova *et al.*, 2009]. Based on the approach by Sheen *et al.* [2012] using the CMPs to estimate the in-plane wave velocity, Tang *et al.* [2014b] designed an improved method specific for the near-surface reflectors using the COGs (common offset gathers).

The principle of the apparent velocity estimation along a survey line is illustrated in Figure 4a with the assumption of uniform vessel velocity. For the given coordinate system with the origin at the second shot ( $s_2$ ), the relationships and velocity ( $V_{seis}$ ) are expressed as:

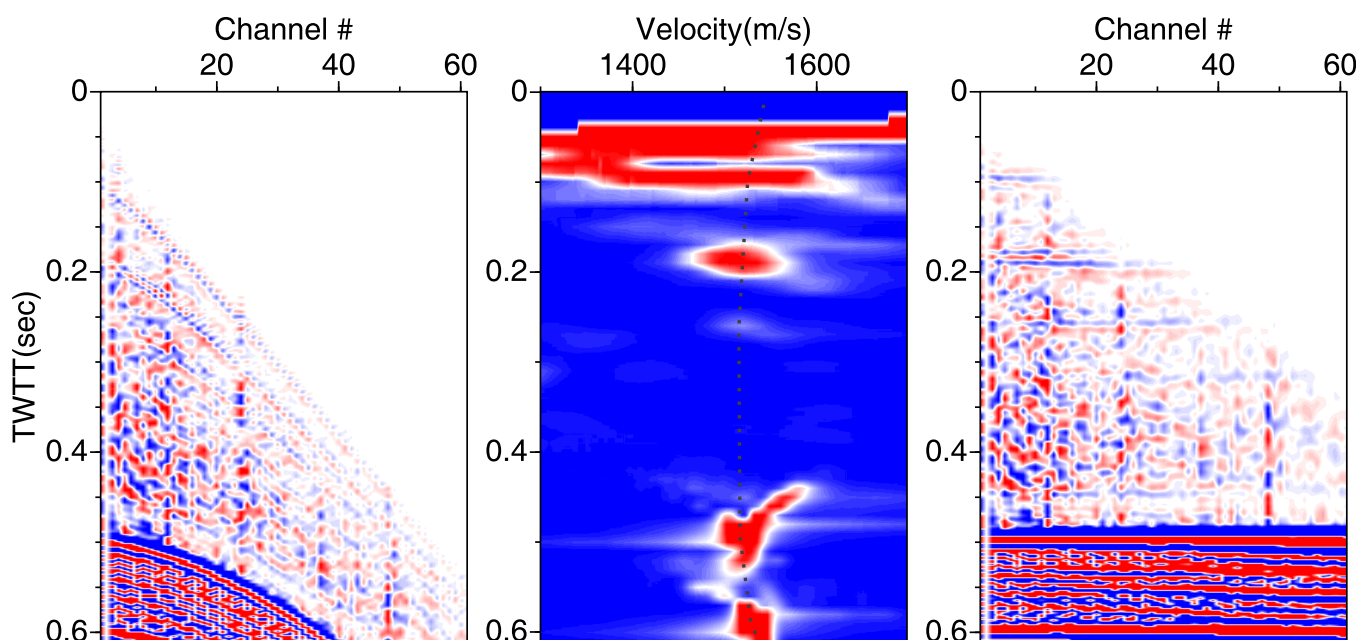


**Figure 3.** Velocity analysis example from a super gather at 88.5 km along Line 1 (left) to derive the acoustic velocity (dash line, middle), which is used for NMO correction (right).

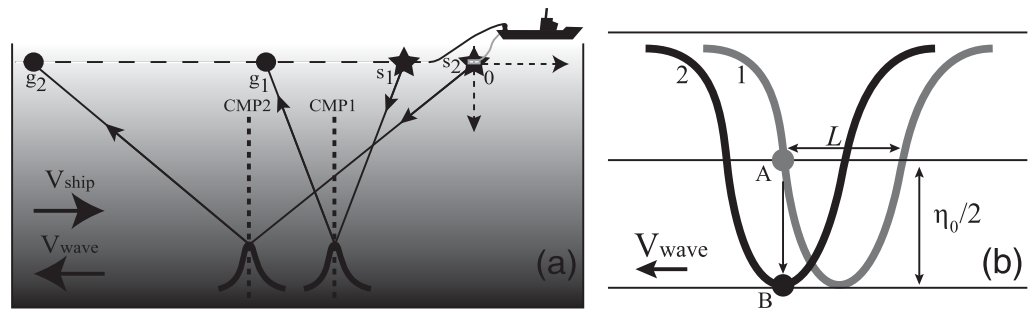


**Figure 4.** Diagrams showing how velocities are measured from the seismic data. (a) Sketch of marine multichannel seismic acquisition and spatial relation with a moving wave. Lines with arrows are the seismic rays reflected from the crest (CMP1 and CMP2, dashed lines) of the same wave (thick curve) at two phases. Dashed arrows are the reference coordinate with  $s_2$  as the origin. (b) Mean vertical velocity of the particle motion from A to B is  $w = \eta_0 V_{wave} / L$  when the ISW moves from phase 1 to phase 2. This figure is modified and combined from Tang et al. [2014b, supporting information]. Figure courtesy of Nature Publishing Group.

$$\begin{cases} CMP2 = -(g_2 * dg + ofs_0) / 2 \\ CMP1 = -\frac{(g_1 * dg + ofs_0)}{2} - (s_2 - s_1) ds \\ V_{seis} = \frac{CMP2 - CMP1}{T} = -\frac{(g_2 - g_1) dg - 2(s_2 - s_1) ds}{2(s_2 - s_1) dt} \end{cases}, \quad (1)$$

where  $(s_1, g_1)$  and  $(s_2, g_2)$  are source-receiver pairs that capture the crest/trough of the moving internal waves at midpoint CMP1 and CMP2, respectively;  $dg$ ,  $ds$ ,  $ofs_0$  are the receiver interval, shot interval, and nearest offset, respectively;  $T$  is the time difference between  $s_1$  and  $s_2$  estimated from the shot time interval  $dt$ . More explanations and examples can be found in Tang et al. [2014b]. It should be noted that the  $V_{seis}$  derived here is the apparent velocity in the direction of the profile and needs to be corrected to the actual velocity that depends on the actual wave direction which could be discovered from satellite image.

In the previous work [Tang et al., 2014b], the minimum value at the wave’s trough was tracked to derive the phase velocity. Because of the shape of the wave the tracking of this location is not very accurate which impacts the ability to define the wave’s velocity. In this study, we picked the front flank of the waveform at the zero-crossing point as this is more sensitive to the movement and thus decreases the uncertainty of the measurement and hence the uncertainty in the wave’s velocity.

Figure 5 shows an example of the improved method using the front flank rather than just one point used in the previous study [Tang et al., 2014b]. After tracking the horizons from the prestack COGs (Figure 5a), we found the best shot-to-receiver slope with the minimum standard deviation (Figure 5d) to the mean waveforms (Figure 5e) using the grid search method (Figure 5b) to make sure the waves are well aligned (Figure 5c). In this example, the best shot-to-receiver slope is the black line corresponding to a velocity of 1.53 m/s. The dashed line represents a static water with a wave velocity of zero as a reference. In the conventional processing procedure, the movement of internal waves are ignored and the seismic traces within any CMP gather will simply stacked and the waveforms will be deformed [Vsemirnova et al., 2009].

In order to estimate the velocity error, 10 groups of randomly selected horizons (gray, Figure 5c) from the whole data set (Figure 5a) were used to derive the phase velocities. This process is similar to the so-called data splitting strategy [Faraway, 1998], which mimics the repeated observation of the wave 10 times using different receivers. Therefore, the standard error of the 10 outputs is treated as the error of the phase velocity.

The mean vertical velocities ( $w$ ) of ISWs were also estimated as shown in Figure 4b from seismic image using the relation [Tang et al., 2014b]:

$$w = \eta_0 V_{seis} / L, \quad (2)$$

where  $\eta_0$  is the amplitude of ISW,  $L$  is the half width of ISW, i.e., a horizontal distance over which the amplitude decreases to  $\eta_0/2$ .

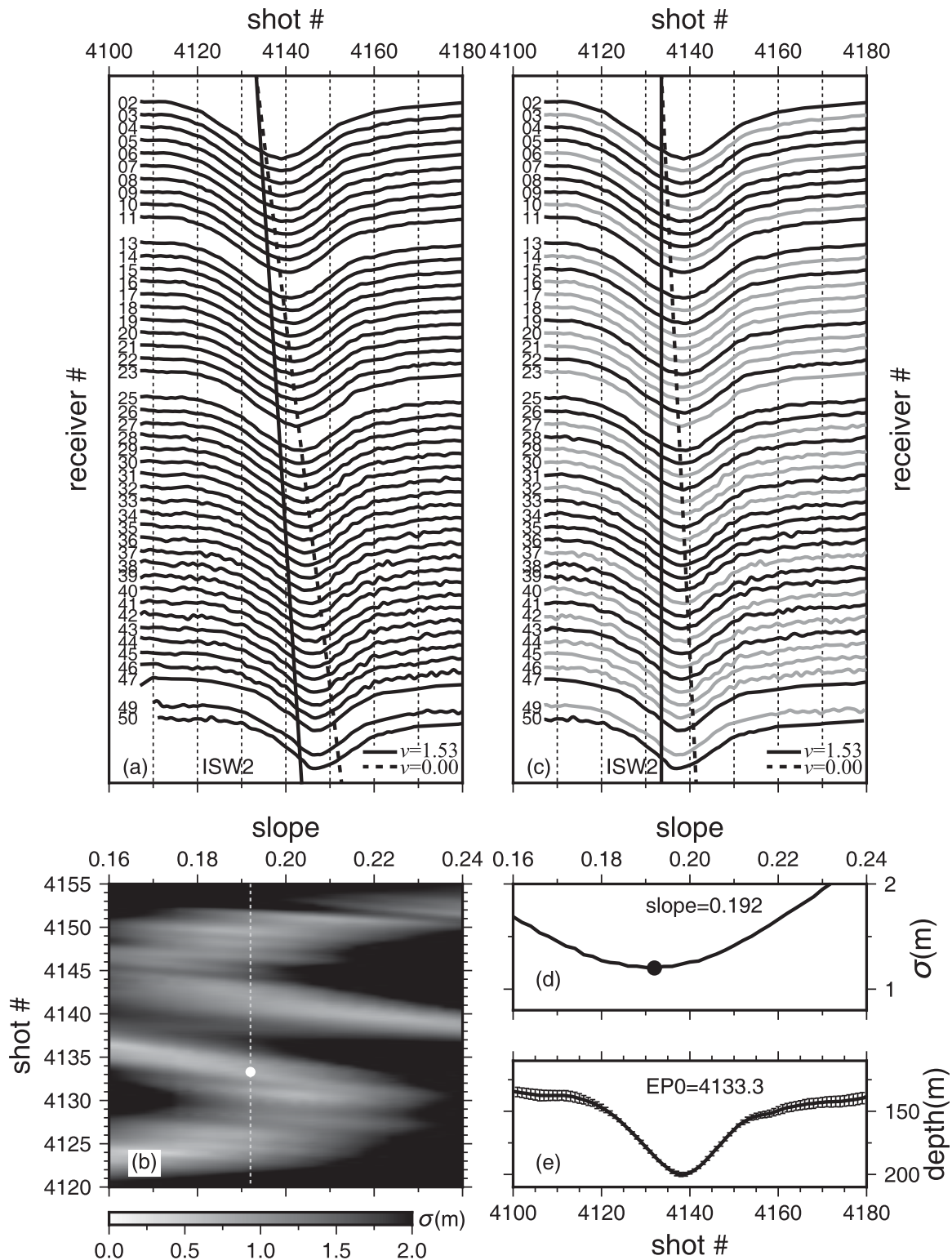


**Figure 5.** Phase velocity estimation for an ISW. (a) Horizons tracked from COGs. Black and dash lines correspond to the moving velocities of 1.53 m/s (best slope) and 0 m/s, respectively. (b) Distribution of standard deviations to the mean amplitudes at each shot for each varying shot-to-receiver slope. White line and dot are the best slope and reference shot with minimum standard deviation, respectively. (c) Corrected horizons along the best slope (black line). Dashed line corresponds to the nonmotion wave. Black (gray) curves are the randomly selected (unselected) horizons for slope calculation. (d) Sum of Figure 5b within the front flank shot ranges of 4120–4120. (e) Sum of the corrected horizons Figure 5c with standard deviation (bars).

2.4. Satellite Imagery

Remote sensors aboard satellites provide the images of ISWs, such as SAR (Synthetic Aperture Radar), ASAR (Advanced SAR), and MODIS (Moderate Resolution Imaging Spectroradiometer) data [Guo and Chen, 2014]. In this study, the data from MODIS sensors flown on two NASA spacecraft (Terra and Aqua) were used to image the sea surface appearance of the ISWs. True color images with lateral resolution of 250 m were created by the software Modis-TrueColor [Gumley et al., 2010]. Fortunately, the weather was clear enough to track the ISWs.

From the satellite images, we first confirmed that the imaged ISWs were the same wave packets as imaged by the seismic method. The mean travel velocity can be measured from the space-time difference between the satellite and seismic observations. A reasonable propagation velocity of 1–2 m/s is a good indication of the same packet near Dongsha Plateau. Further, with the help of the wavefronts of ISWs on the satellite image, wave directions were estimated and used to correct the apparent velocities derived from the seismic data ( $V_{sa}$ ) along the seismic profiles:

$$V_{seis} = V_{sa} * \cos(A), \tag{3}$$

where  $A$  is the angle between ISW propagation and seismic line heading. However, as the seismic profile orientation was chosen to be orthogonal to the expected ISW's this correction is negligible.

2.5. Hydrographic Data

During the cruise, 36 XBTs of probe-type D5 [Zhang et al., 2012] were deployed along the survey lines (Figure 1b) at an approximate 10 km spacing, with a few more closely deployed over ISW regions.

The nonlinear phase velocity of ISW can be calculated analytically from the temperature and salinity according to mathematical model with the help of a known ISW amplitude. Therefore, the salinity has to be estimated from the temperature of XBT casts. We used a nonlinear neural network algorithm [Ballabrera-Poy et al., 2009] to derive the temperature-salinity relation using the legacy CTD casts as presented by Kormann et al. [2011] and Biescas et al. [2014]. The estimated standard deviations from the absolute differences using the neural network are below 0.1 and 0.025 psu at 60 and 200 m, respectively. Once the salinity data were estimated, other quantities such as density and buoyancy frequency were calculated. According to the salinity contribution of ~6% to the density at 100 m depth of this study region, the error of the salinity will not affect the buoyancy frequency significantly.

For the continuously stratified fluid  $N(z)$  without background shear current, both KdV (Korteweg-de Vries) equation:

$$\frac{\partial \eta}{\partial t} + (c + \alpha \eta) \frac{\partial \eta}{\partial x} + \beta \frac{\partial^3 \eta}{\partial x^3} = 0 \tag{4}$$

and eKdV (extended KdV) equation:

$$\frac{\partial \eta}{\partial t} + (c + \alpha \eta + \alpha_1 \eta^2) \frac{\partial \eta}{\partial x} + \beta \frac{\partial^3 \eta}{\partial x^3} = 0 \tag{5}$$

were used to predict the waveform parameters of ISWs analytically [Grimshaw et al., 2002; Ramp et al., 2004; Zhao et al., 2012]. In equations (4) and (5),  $\alpha$  and  $\alpha_1$  are the quadratic and cubic nonlinear parameters, respectively;  $\beta$  is the dispersive coefficient;  $c$  is the first-mode linear phase velocity, which is derived from the Sturm-Liouville equation:

$$\frac{d^2 W(z)}{dz^2} + \frac{N^2(z)}{c^2} W(z) = 0, \tag{6}$$

with a zero-boundary condition  $W(0) = W(H) = 0$  for the eigenfunction  $W(z)$  [Fliegel and Hunkins, 1975]. The theoretical ISW solutions of equations (4) and (5) are

$$\begin{cases} \eta(x, t) = \eta_0 \operatorname{sech}^2\left(\frac{x-vt}{\Delta}\right) \\ \Delta^2 = \frac{12\beta}{\alpha\eta_0} \\ V_{KdV} = c + \frac{\alpha\eta_0}{3} \end{cases} \tag{7}$$

and

$$\left\{ \begin{array}{l} \eta(x, t) = \frac{A}{1 + B \cosh\left(\frac{x-vt}{D}\right)} \\ B = 1 + \frac{\alpha_1}{\alpha} \eta_0 \\ A = \eta_0(1 + B) \\ D^2 = \frac{6\beta}{\alpha A} \\ V_{eKdV} = c + \frac{\alpha A}{6} = V_{KdV} + \frac{\alpha_1 \eta_0^2}{6} \end{array} \right. \quad (8)$$

where  $\Delta$  and  $D$  are the characteristic widths, and  $V_{KdV}$  and  $V_{eKdV}$  are the nonlinear phase velocities from KdV and eKdV model, respectively.

It is straightforward to compute the vertical velocities of particle motion from the analytical solutions (7) and (8) via partial derivative  $w(x) = \partial\eta(x, t) / \partial t|_{t=0}$ :

$$w(x) = -2 \frac{V_{KdV} \eta_0}{\Delta} \operatorname{sech}^2\left(\frac{x}{\Delta}\right) \tanh^2\left(\frac{x}{\Delta}\right) \quad (9)$$

and

$$w(x) = \frac{B V_{eKdV}}{AD} \eta^2\left(\frac{x}{D}\right) \sinh\left(\frac{x}{D}\right) \quad (10)$$

for the KdV and eKdV models, respectively [Trevorrow, 1998; Teague et al., 2011].

### 3. Results

#### 3.1. Images of ISW Packets

At least seven packets of ISWs were encountered during the seismic cruise. After careful processing, two representative wave packets located at northeast and northwest of Dongsha Island where the seabed shoals from ~370 to ~300 m were selected for further analysis (Figure 6). With a mean vessel velocity of 5.0 knots, it took 2–2.5 h to complete these two subsections.

Figure 6a depicts a prototypical rank-ordered ISW packet (G1) with at least five well-shaped solitons plus a few other deformed ones too. All of them are treated as first-mode depression waves. For the leading soliton around 73–74 km, only the front flank was imaged because of the rear flank (74–77 km) was lost in increased receiver noise. This noise was produced because the streamer was uplifted from 5 m tow-depth to the sea surface by the strong upward restoring force of the soliton. The MODIS image captured this packet twice (Figure 7): the first occurrence was at 03:00 on 12 July 2014 in the eastern deep basin; the second occurrence was at 05:15 the next day on Dongsha Plateau. The measured distance is 259 km, which corresponds to the wavelength of a diurnal internal tide in the deep basin [Guo and Chen, 2014]. The derived mean velocity 2.74 m/s is also consistent to the nonlinear ISW phase velocity over the basin region [Zhao and Alford, 2006; Jackson, 2009].

A more complex wave packet (G2) with many wave cycles was imaged to the northwest of Dongsha Island (Figure 6b). Although the polarity of leading solitons (41–45 km) is still depression as the water bottom shoals to ~300 m, their waveforms have been irregularly deformed. Examining the complex finescale structure shows that the waves might be collapsing by changing their stratification and/or by lateral refraction of the northern crest arm (Figure 8) [Li et al., 2013]. For some waves the so-called “kink-antikink” flat-top shape was forming or formed [Pelinovskii et al., 2000; Apel et al., 2007]. After the passing of the leading wave, the upper mixed layer is deeper, then the elevation waves with reversed polarity develop (46–56 km), with occasional depression waves (e.g., ~51 km). After 56 km, small depression waves appear as the stratification is restored. The G2 packet was also captured by the NASA Aqua satellite and shows the refracted packet signature north of Dongsha Island (Figure 8).

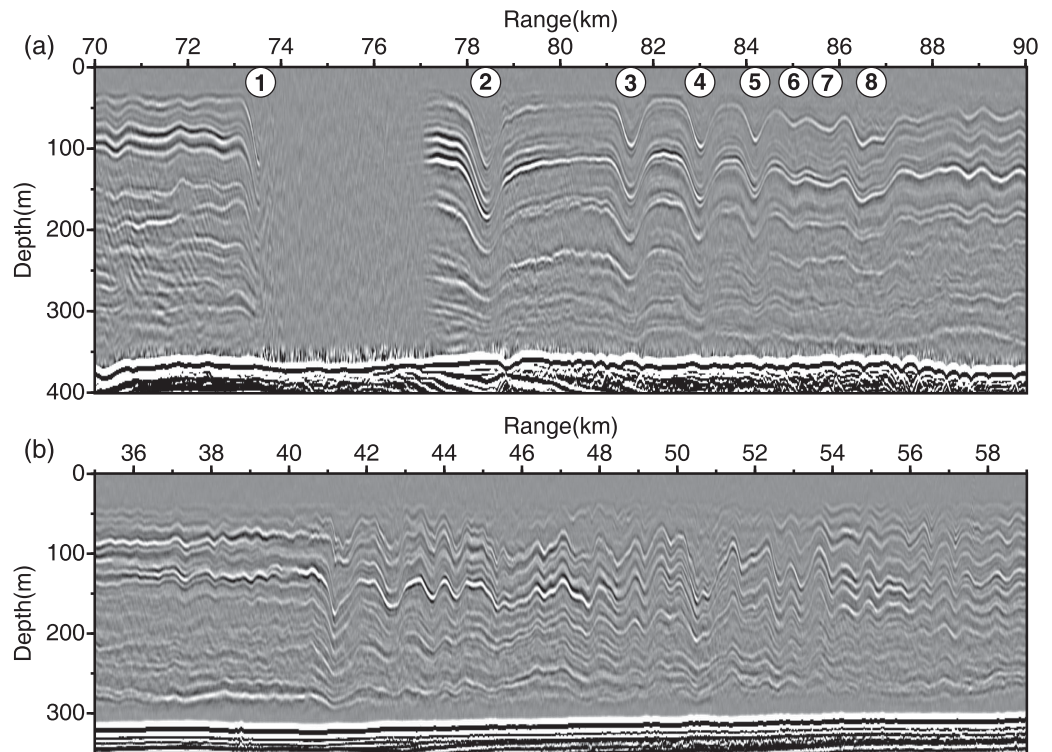


**Figure 6.** Seismic images of two ISW packets on Dongsha Plateau. (a) A rank-ordered soliton packet (numbered) northeast of Dongsha Island on subsection SO1E. The blank part at 74–77 km range is because of the noise contamination of the uplifted seismic streamer to the sea surface driven by the upward velocity on the rear flank of the leading ISW. (b) A complex ISW packet northwest of Dongsha Island on subsection SO1N.

Using seismic oceanography, it is easy to observe the shapes of ISWs and the quality of the seismic images provide an efficient way to map the finescale feature of ISWs. For example, the G2 packet (Figure 6b) shows a complex ISW packet with combination of both elevation and depression waves, which were captured by seismic observation for the first time. The seismic oceanography method can also be used to determine

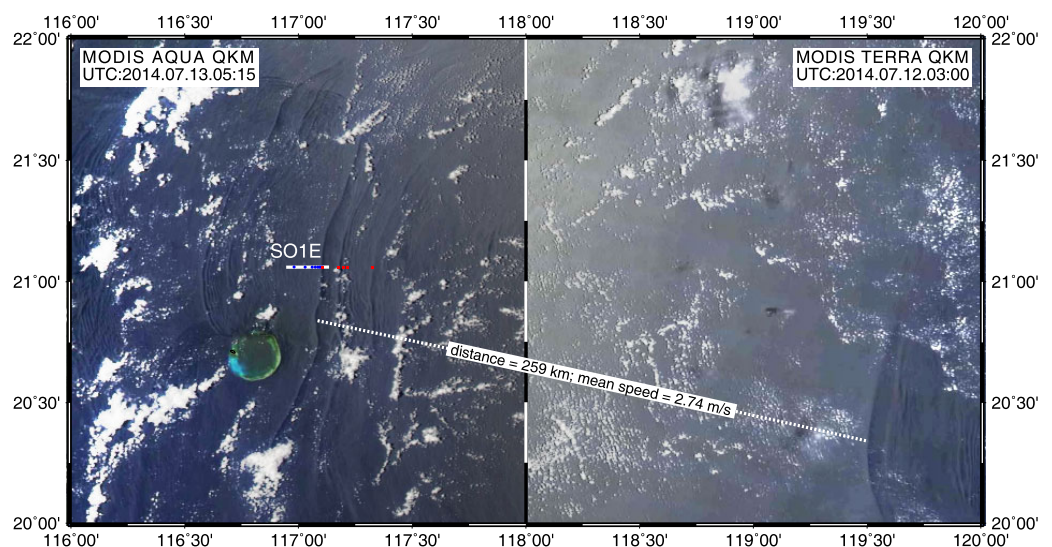


**Figure 7.** Two MODIS images of the ISWs acquired by (left) NASA Aqua and (right) Terra satellites with around 1 day time lag. White line is the seismic subsection SO1E of Figure 6a starting at 07:03 UTC. Blue and red dots are the locations of solitons imaged by seismic and satellite observations, respectively. A possible propagation path (white dashed line) of the wave crest with measured distance and mean velocity are noted.

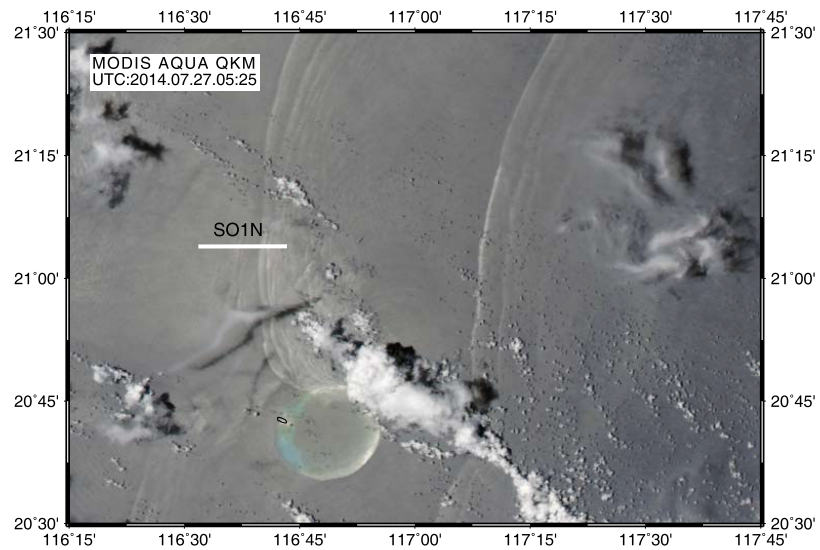


**Figure 8.** MODIS images of the ISWs acquired by NASA Aqua satellite at 05:25 UTC on 27 June 2014. White line is the seismic subsection SO1N of Figure 6b starting at 06:15 UTC.

other physical quantities. In the rest of this study, we will focus on the prototypical ISW packet G1 to extract quantitative information and corroborate it with other independent observations.

### 3.2. Characteristics of ISW Packet

Eight waves of the rank-ordered ISW packet G1 (Figure 6a) were treated as the individual solitons and their parameters were determined from satellite, seismic, and hydrographic data, although sixth and seventh ISWs were not well-developed or not very convincing. The observed/estimated quantities about wave-shapes, horizontal propagation velocities, and vertical velocities are presented in Table 1, as well as the detailed intermediate variables listed in Table 2.

#### 3.2.1. Waveshapes

It is possible to measure the scale parameters of these solitons and extract their waveforms from the seismic image. Amplitude decreases gradually from 80 to 16 m for the front seven solitons then increases to 35 m for the last one. The wavelength parameter  $L$  (full width of ISW trough at half amplitude) shows the similar variation except for the leading soliton, whose width is less than 3/5 of the second soliton. Generally, these trends are in accordance with the surface signature of the satellite image (Figure 7), i.e., high/wide/steep-sided waves have more significant brightness contrasts and spatial extensions. In particular, it is difficult to locate the fifth soliton on the MODIS image, possibly indicating a newly developing soliton.

An effective way to check the scale length given the local stratification is by using the weakly nonlinear theory of KdV which predicts that the wavelength parameter  $L$  is 1.76 times of the characteristic width  $\Delta$  for

**Table 1.** Observed and Derived Parameters of the ISWs<sup>a</sup>

ISW#	EP#	x (km)	$V_{ship}$ (m/s)	$\eta_0$ (m)	wd (m)	La (m)	L (m)	$\Delta$ (m)	$L/\Delta$ (1.76) <sup>b</sup>	$V_{sat}$ (m/s)	$V_{seis}$ (m/s)	$V_{KdV}$ (m/s)	$V_{eKdV}$ (m/s)	$W_{seis}$ (cm/s)	$W_{KdV}$ (cm/s)	$W_{eKdV}$ (cm/s)
1	3944	73.5	2.18	80	370	264	431	247	1.74	1.66	$1.68 \pm 0.15$	1.53	1.92	$31.2 \pm 2.8$	28.1	58.2
2	4140	78.4	1.80	76	363	496	761	259	2.94	1.62	$1.72 \pm 0.05$	1.51	1.80	$17.2 \pm 0.5$	25.1	46.6
3	4264	81.5	2.25	54	364	400	612	316	1.94	1.34	$1.29 \pm 0.04$	1.42	1.55	$11.4 \pm 0.3$	13.8	20.1
4	4323	83.0	2.25	54	370	384	553	332	1.67	1.28	$1.20 \pm 0.06$	1.47	1.59	$11.7 \pm 0.6$	13.6	20.1
5	4370	84.2	2.35	40	370	322	464	395	1.17		$1.10 \pm 0.04$	1.53	1.59	$9.5 \pm 0.4$	8.8	11.4
6	4404	85.0	2.30	20	370	332	421	550	0.77		$0.88 \pm 0.13$	1.43	1.44	$4.2 \pm 0.6$	3.0	3.4
7	4434	85.8	2.25	16	370	340		617				1.41	1.42		2.1	2.4
8	4462	86.5	2.10	35	370	380	608	410	1.48	1.78	$1.81 \pm 0.11$	1.49	1.54	$10.4 \pm 0.6$	7.3	9.1

<sup>a</sup>EP, seismic shot number; x, location on the seismic line;  $V_{ship}$ , average ship speed;  $\eta_0$ , amplitude; wd, water depth; L (La), (apparent) full width of the trough at half amplitude from seismic image;  $\Delta$ , characteristic width using KdV model;  $V_{sat}$ , phase speed from satellite observation;  $V_{seis}$ , phase speed from seismic observation;  $V_{KdV}$  ( $V_{eKdV}$ ), phase speed from KdV (eKdV) model;  $W_{seis}$ , vertical speed from seismic observation;  $W_{KdV}$  ( $W_{eKdV}$ ), vertical speed from KdV (eKdV) model.

<sup>b</sup>The number 1.76 is the analytical ratio of the full width L at half amplitude to the characteristic width  $\Delta$  of KdV model.

**Table 2.** Detailed Parameters in Phase Speeds (m/s) Estimations Using Satellite, Seismic, KdV, and eKdV Methods

ISW#	Satellite <sup>a</sup>			Seismic <sup>b</sup>			KdV <sup>c</sup>					eKdV <sup>d</sup>				
	dist(m)	dt(s)	V <sub>sat</sub>	EPO	slope	V <sub>seis</sub>	c	α	β	Δ	V <sub>KdV</sub>	α <sub>1</sub>	A	B	D	V <sub>eKdV</sub>
1	12,991	7,831	1.66	3933.9	0.174 ± 0.006	1.68 ± 0.15	1.13	-0.0151	6,152	247	1.53	3.66E-04	315	2.93	88	1.92
2	15,835	9,791	1.62	4133.2	0.193 ± 0.004	1.72 ± 0.05	1.15	-0.0144	6,116	259	1.51	3.02E-04	273	2.59	97	1.80
3	14,758	11,031	1.34	4259.7	0.200 ± 0.002	1.29 ± 0.04	1.17	-0.0140	6,263	316	1.42	2.64E-04	163	2.02	129	1.55
4	14,918	11,621	1.28	4314.2	0.196 ± 0.004	1.20 ± 0.06	1.22	-0.0138	6,841	332	1.47	2.49E-04	161	1.98	136	1.59
5		12,091		4361.8	0.197 ± 0.004	1.10 ± 0.04	1.34	-0.0145	7,567	395	1.53	2.22E-04	104	1.61	173	1.59
6		12,431		4395.1	0.195 ± 0.007	0.88 ± 0.13	1.33	-0.0147	7,423	550	1.43	2.15E-04	46	1.29	257	1.44
7		12,731					1.33	-0.0148	7,484	617	1.41	2.44E-04	36	1.26	290	1.42
8	23,184	13,011	1.78	4452.3	0.164 ± 0.005	1.81 ± 0.11	1.32	-0.0150	7,331	410	1.49	2.27E-04	89	1.53	182	1.54

<sup>a</sup>Satellite method, the mean velocities derived from the spatial (dist) and temporal (dt) spans between two observations by satellite and seismic.

<sup>b</sup>Seismic method, EPO and slope are the reference shot number and shot-to-receiver ratio in deriving the phase speed V<sub>seis</sub> of ISWs, respectively.

<sup>c</sup>See equations (4) and (7).

<sup>d</sup>See equations (5) and (8).

the KdV solution. From the ratio of  $L/\Delta$ , the leading soliton best fits the KdV prediction and then the fourth and third solitons, in that order. A higher  $L/\Delta$  ratio is an indicator of lower nonlinearity or higher dispersion. This suggests that the second soliton with the ratio of 2.94 might be prone to dispersion and disintegration. For the eighth wave, the  $L/\Delta$  ratio 1.48 is probably underestimated since we used the front flank to estimate the length of  $L = 608$  m rather than the whole length of  $L = 1368$  m, which will result a  $L/\Delta$  ratio of 3.24. Such a high  $L/\Delta$  ratio might explain the complex waveshape caused by likely disintegration [Grimshaw et al., 2010].

There is no simple ratio between the wavelength parameter  $L$  and eKdV characteristic width  $D$ , since it is adjusted by the parameter  $B$  (equation (8)) via  $L/D = 2acosh(2 + B^{-1})$ . Therefore, it is not straightforward to compare the fitness of the results only if the whole waveforms are illustrated. A comparison for the eKdV and seismic results will be shown in the discussion part of this study and compared to the KdV solutions.

### 3.2.2. Wave Transmission

The phase velocity is one of the most important kinematic parameters depicting the horizontal movement of the ISW crest. Four group of phase velocities were estimated from the data sets. The parameters used for the phase velocity estimations were detailed in Table 2, and the final results were both listed in Tables 1 and 2 and illustrated in Figure 9a.

The phase velocity from satellite image needs constraint of the seismic data as it is the mean velocity between the two different observations. Therefore, this velocity might be different from the transient velocity obtained using the seismic or in situ hydrographic observations if the topography or stratification changes considerably along the path. However, this effect is insignificant because of the relatively even topography and stratification on Dongsha Plateau. No estimates of velocity were measured for solitons 5–7 because they were too weak to identify on the MODIS image (Figure 7). Phase velocities were decreasing in order from 1.66 to 1.28 m/s for the first four solitons (Figure 9a). The soliton 8 has a higher mean velocity of 1.78 m/s, probably because the average bathymetry (~600 m) was deeper along its path (Figure 1).

The transient phase velocities from seismic data were derived in a 50 receiver spatial window which was equivalent to a time window of 4 min. We can see that the phase velocities from seismic  $V_{seis}$  is very close to the mean velocities from satellite  $V_{sat}$ , which fall into the error of  $V_{seis}$ . The overall trend of  $V_{seis}$  is the same to  $V_{sat}$ : systematically decreasing for the front solitons followed by the final wave with a higher velocities of  $1.81 \pm 0.11$  m/s. The phase velocities of fifth and sixth waves were estimated successfully from the seismic data, but failed for the seventh wave. This is because its front flank is nearly flat at ~120 m depth and thus provides no feature on which to determine velocity. Three main factors affect the uncertainties of  $V_{seis}$ : first is the noise of seismic data, e.g., the first soliton; second is the steepness of the flank, e.g., the sixth wave; and the third is the length of the flank, e.g., the sixth and eighth waves.

Phase velocities for the analytical predictions were computed from the local mean of the stratification (e.g., Figures 10a and 10b) provided from the XBT data. Through solving the KdV equation (4) or eKdV equation (5), analytical solutions of ISWs were derived (Tables 1 and 2 and Figure 9). The phase velocities from the KdV model are stable and varying around  $1.47 \pm 0.6$  m/s. The variation is larger for the eKdV solution

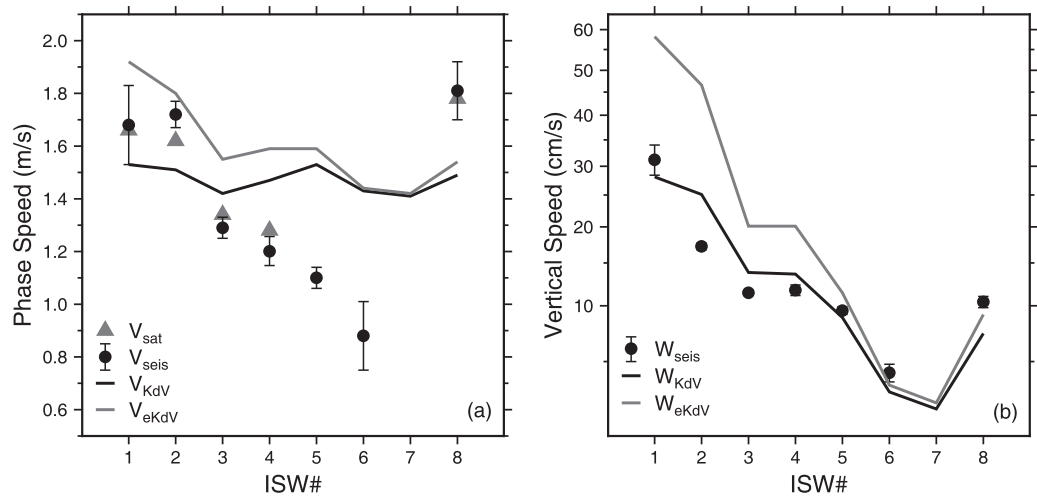


**Figure 9.** (a) Phase velocities of the ISW packet derived from satellite (gray triangle), seismic (black dots with error bars), KdV model (black line), and eKdV model (gray line). (b) Vertical velocities estimated from seismic (black dots with error bars), KdV model (black line), and eKdV model (gray line).

ranging from 1.92 to 1.42 m/s. The velocities from eKdV model are always higher than from KdV model because of the positive cubic nonlinear parameters  $\alpha_1$  (Table 2) according to equation (8). In general, the KdV solutions are closer to the values from satellite and seismic methods than the eKdV solutions. This is because these solitons have small  $\eta_0/h_2$  which is appropriate for KdV model but the stratification is far from eKdV satisfying condition with  $0.4 < h_1/(h_1+h_2) < 0.6$  based on the simplified two-layer system of the study region [Michallet and Barthelemy, 1998; Grue et al., 1999]. Here  $h_1$  and  $h_2$  are the upper and lower layer thicknesses, respectively.

### 3.2.3. Vertical Particle Motion

While much attention is given to the phase velocities of the ISW propagation [e.g., Ramp et al., 2004; Jackson, 2009], the vertical velocities are less extensively studied [Chang et al., 2011; Zhao et al., 2012]. There is a practical implication of this for this study since the streamer was uplifted to the sea surface by the strong vertical movement associated with the ISW. So for a period no useful data were recorded until depth control of the receiver could be regained.

The last three columns in Table 1 show the estimated vertical velocities from the seismic data (Figure 4b) and the KdV and eKdV models. Figure 10e shows an example of how the mean velocities are analytically measured from the half-width point to the trough. When derived from seismic data, the vertical velocities  $W_{seis}$  decrease progressively from the first to the sixth soliton with the values ranging from ~30 to ~4 cm/s. But the eighth soliton is stronger than its adjacent foregoing waves. The greatest value is found for the leading soliton whose vertical velocity is nearly twice that of the second soliton, even though the amplitude and phase velocity are almost identical. Here the steepness of the flank is the dominating factor inducing the abrupt jump of the vertical velocity. The velocity of 30 cm/s is outside the response time of the streamer's self-stabilization system to maintain the receiver's depth hence the reason why it surfaced.

The predicted vertical velocities from KdV model  $W_{KdV}$  are close to  $W_{seis}$  (Table 1 and Figure 9), with a typical discrepancy of 3 cm/s. The velocities  $W_{eKdV}$  were largely overestimated by a factor of two compared with  $W_{KdV}$  for the first four solitons. From the vertical velocity estimation, the KdV model is more suitable than the eKdV model for this study.

## 4. Discussions

### 4.1. Performance of Seismic Observation

From this and previous observation of ISWs [Tang et al., 2014b], it can be concluded that the seismic oceanography is an efficient and effective way to detect the ISWs in a near-surface region below 40, which was considered to be a challenging zone for the conventional seismic technique [Piété et al., 2013; Biescas et al., 2014]. To ensure high-quality seismic data, there are three primary requirements: (1) optimizing air gun

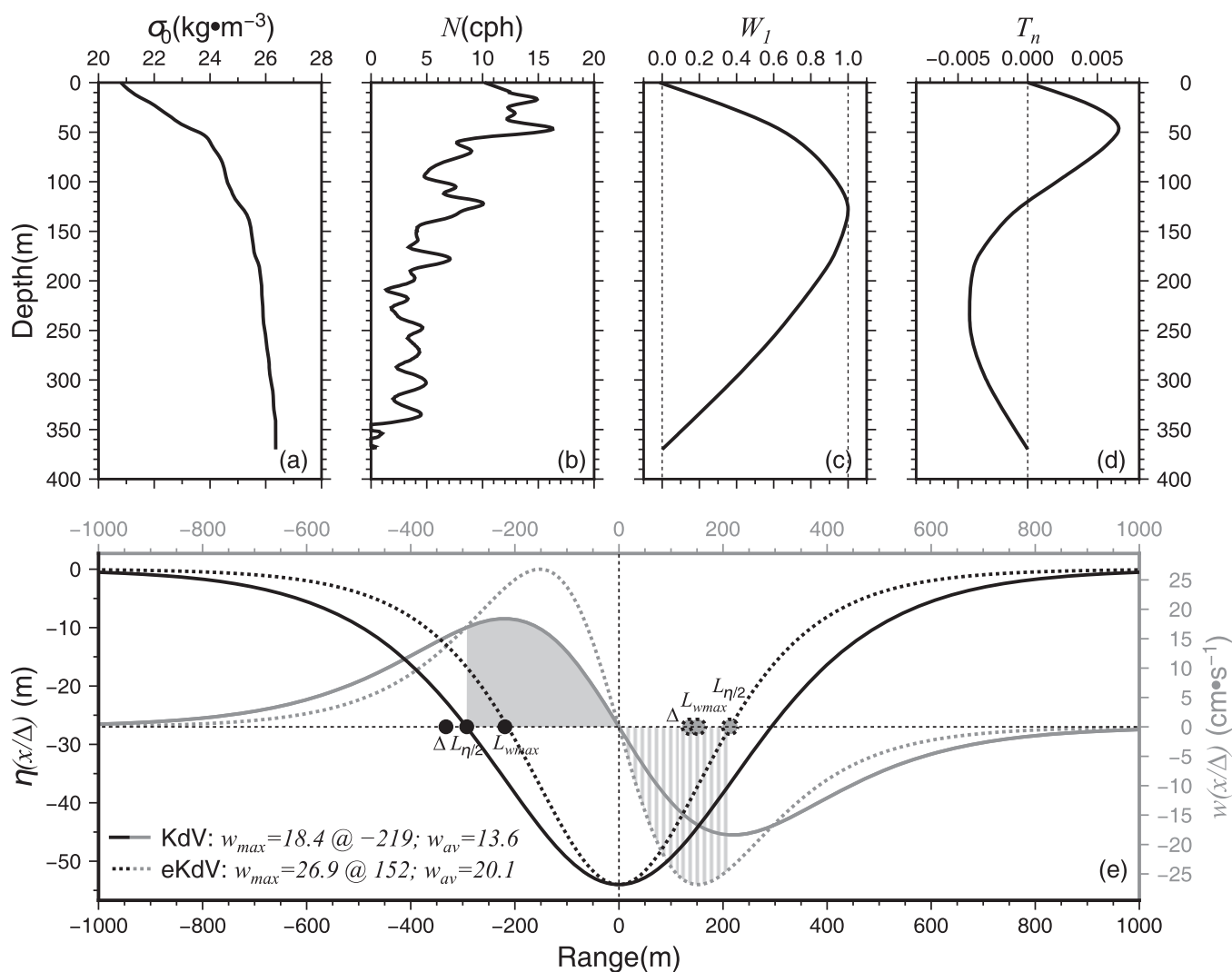


**Figure 10.** Example of model predictions for the fourth soliton. (a) Local mean potential density. (b) Buoyancy frequency. (c) Normalized first-mode eigenfunction. (d) Nonlinear correction to the mode eigenfunction. (e) Double-axis plot of the predicted waveforms (black) and vertical velocities (gray). Solid and dotted lines are for the KdV and (eKdV) models, respectively. Three black (gray) dots are characteristic with  $\Delta$  ( $D$ ), half-width  $L_{\eta/2}=L/2$ , and maximum vertical velocity point  $L_{wmax}$ , respectively, for the KdV (eKdV) model. The gray filled (line) shade is for integrating the mean vertical velocity of KdV (eKdV) model from the half-width point to the trough corresponding to the seismic method.

type and array so the direct wave can be suppressed; (2) a small nearest offset ( $<100$  m) for minimizing the blank zone; and (3) a mid-size vessel for reducing the ambient noise. In this study, the R/V *SHIYAN2* provided a good platform for the seismic data observation.

Choosing a right time is also important for observing the periodical large amplitude ISWs [Ramp *et al.*, 2004; Zheng *et al.*, 2007; Du *et al.*, 2008]. The occurrence frequency tells us that the combination of summer time and spring tides are the optimum conditions to capture large amplitude and long train ISWs. As occurred for this study, i.e., both ISWs packets were detected during spring tides in the summer of 2014 (Figure 11). ISWs could still be detected during the neap tides but the smaller amplitudes [Tang *et al.*, 2014b].

Seismic observation offers new opportunities for mapping shallow finescale structures (Figure 6). Its ability to capture a snapshot enables the spatial relationships between individual solitons and ambient waters to be determined. The full-depth image provides a means to view of interactions between the water and sea bottom topography. The prestack seismic data contain additional information which is still to be fully exploited. The resolution of 10 m for the seismic image is typically higher than the conventional mooring observation with 1–3 min sample rate (horizontally  $\sim 50$ – $500$  m) and  $\sim 20$  m vertical sensor interval [Ramp *et al.*, 2004, 2010].

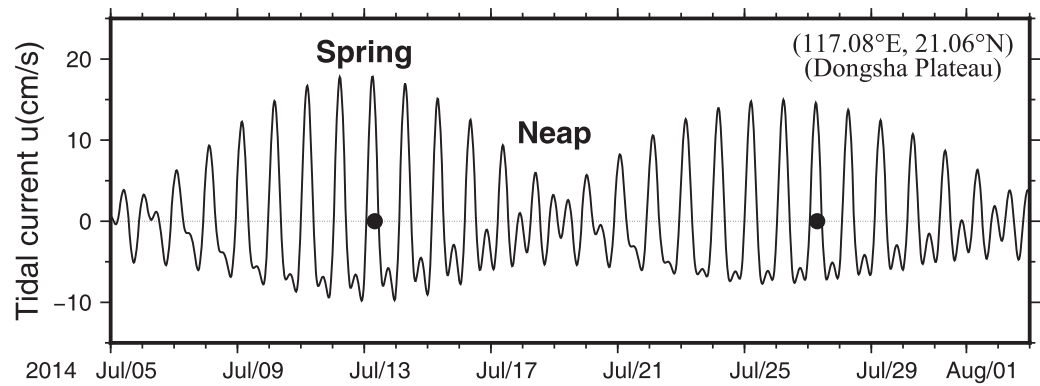


**Figure 11.** Model-predicted barotropic tidal current on Dongsha Plateau. The left and right black dots are the seismic acquisition time of the ISW packets of Figures 6a and 6b, respectively. Both surveys were conducted near the peaks of the spring tide.

#### 4.2. Corroborating With Other Data

In the primary stage of seismic oceanography for studying ISWs, mutual verification from other independent observations are crucial. We have presented two types of conventional observational data, synchronized satellite and in situ hydrographic data, to test the reliability of seismic observation. In addition, we also have other records, including photos, ship-board radar, and vessel velocity and heading, to further support the location of ISWs. However, we note that we failed to detect the ISWs using a 3.5 kHz echo sounder during this experiment possibly because the frequency we used was too low to detect the ISW fields.

Quantified parameters, such as waveshapes, phase, and vertical velocities, are useful for evaluating the veracity of different observations. We combine these quantities pictorially in Figure 12. Examining the

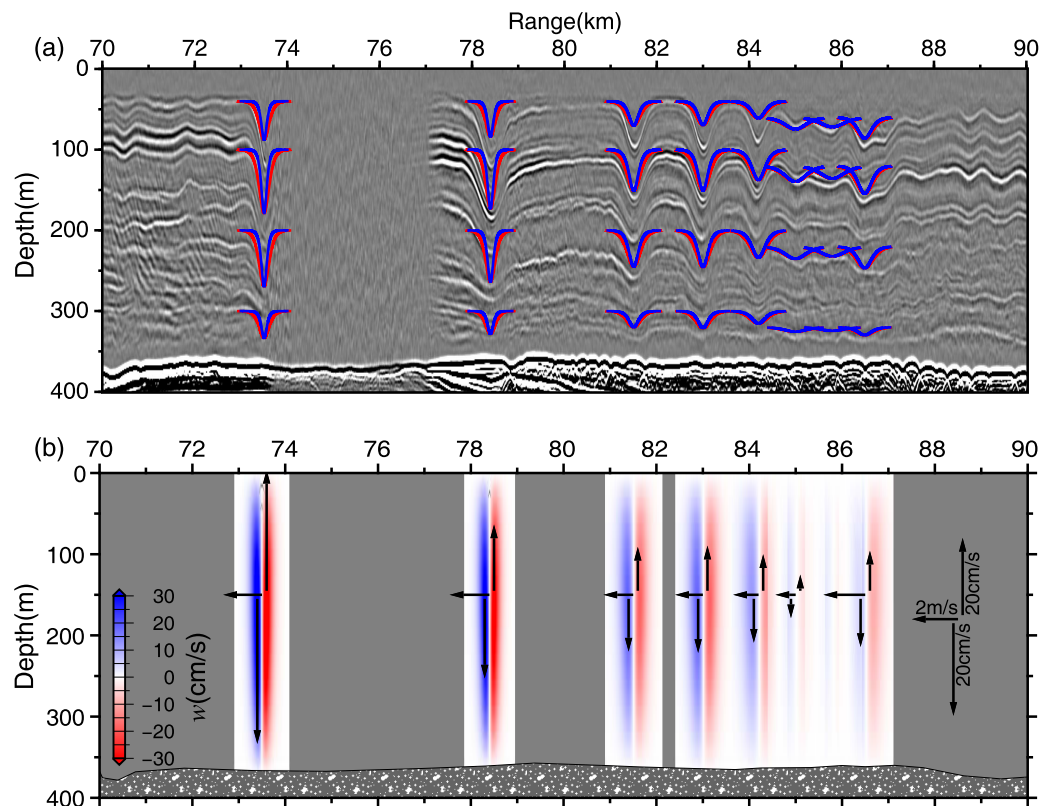


**Figure 12.** A composite figure showing the observed or predicted parameters of ISWs. (a) Seismic-imaged waveforms superposed with analytical waveforms from KdV (red) and eKdV (blue) models. (b) Vertical velocities (vertical arrows) superposed on the analytical vertical velocity fields. Horizontal arrows are the seismically derived velocities  $V_{seis}$ .

waveform shape (Figure 12a), it can be seen the KdV solutions (red) are always closer to the seismic observations than the eKdV (blue) solutions. It is true even for the second soliton, though its phase velocity  $V_{eKdV}$  is with a better match with  $V_{seis}$  than the value obtained from  $V_{KdV}$  (Tables 1 and 2 and Figure 10). This implicates that a single parameter, e.g., phase velocity, may not accurate enough to judge the model's accuracy without consideration of other parameters, such as waveshapes. For the fitting of vertical amplitude of individual solitons, the overall agreement between the model predictions corrected by the first vertical displacement mode (Figure 10c) and seismic observations are satisfactory, except for the shallowest solitons where the discrepancies are large. This might be improved by a fully nonlinear numerical model as shown by *Chang et al.* [2011].

We only present the analytical vertical velocity field of the KdV model in Figure 12b because of its superior agreement with the seismic observation compared to the eKdV model. The mean vertical velocities from the seismic observation are superimposed, as well as the phase velocities, providing a snapshot for the quantified kinematic parameters of the ISW field.

From the independent observations and analyses we can see that: (a) generally, the phase velocities from KdV model are closer to the values from seismic observation than eKdV model, but both are worse than satellite measurements; (b) the performance of the KdV model on waveform shape compared with the seismic image is also better than the eKdV model; and (c) the vertical velocities from KdV model are close to the seismic results, while the eKdV model largely overestimates the parameters. The consistency between the seismic results and KdV predictions further indicates that the KdV model provides accurate predictions for this study. Nevertheless, the background shear or baroclinic currents were not included in this study. The absence of background shear might be significant to the predictions [*Wang and Pawlowicz*, 2011] and it could change the conclusion presented here if it was considered.

By examining the features of the solitons, they can be further characterized into three subgroups, showing the different evolution scenarios. The first subgroup is the leading soliton with fast propagation velocity and largest vertical velocity. The second subgroup ranging from the second to seventh waves show a number of evolutionary characteristics: (1) some solitons might be newborn by nonlinear steepening or dispersing toward the rear of the group, (2) the distance of the train is elongated because of the decreasing velocities for rank-ordered solitons, and (3) isolation of the second soliton from the second subgroup is obvious because of the expanded distance between second to third solitons as seen from the satellite and seismic snapshots (Figures 6 and 7). The last soliton could be regarded as the third subgroup. Besides the deformed waveform, its phase velocity is much faster than the trailing waves of the second subgroup. It is catching up or even overtaking them. The higher velocities determined from both satellite and seismic method are underestimated by both the KdV and eKdV model.

### 4.3. Engineering Implications

Little research has been made on the forces exerted on offshore structures, e.g., oil rigs, by the strong wave-induced horizontal velocities [*Cai et al.*, 2006]. There are hypotheses that the catastrophe of the US Navy Thresher submarine may have been caused by the vertical movement of the ISWs [*Apel et al.*, 2007; V. V. Bulatov and Y. V. Vladimirov, arXiv.org, e-Print Arch. Phys., 0609236, arXiv: 1206.6136, 2012]. Here we report that seismic operation was disturbed by the ISWs uplifting the streamer to the surface with consequential degradation of the solid earth reflections and complete loss of the weak water reflections (Figure 6a). It took  $\sim 20$  min ( $\sim 3$  km) for the streamer to restore to the normal depth. Equally and ISW could drag the streamer downward which may damage the equipment.

The critical vertical velocity for uplifting the 5 m towed streamer to the sea surface is around 17 cm/s at the main thermocline, or approximately  $\sim 75$  m for the critical ISW amplitude. This problem exists in this region because of the presence of ISWs. Theoretically, increasing the streamer depth or the number of depth controlling units may help. Further, the change in ship's velocity caused by the strong horizontal wave-induced current could reduce tension on the streamer and facilitate the vertical movement of the streamer. Therefore, maintaining the vessel velocity may help control streamer lift.

## 5. Conclusions

An optimized seismic cruise was carried out to observe the ISWs on Dongsha Plateau in July 2014 following a first trial in 2012 and a series of rank-ordered soliton trains were captured for the first time. Two ISW

packets from northeast and northwest sides of Dongsha Island were identified after careful seismic data processing. On northeast side of the island with bottom depth of  $\sim 370$  m, a prototypical rank-ordered train with several waves was fully captured. In the shoaling water of  $\sim 300$  m on the northwest side of the island, a more complex packet with combination of depression and elevation waves was imaged for the first time. Both seismic findings were confirmed by satellite observations.

Thanks to the redundancy and high-resolution of seismic acquisition, seismic signals were used to determine several parameters of the ISW packet on the northeast side of Dongsha Island. An improved scheme was applied to derive the transient velocity by including more observed information. Mutual verification from satellite and hydrographic approaches were consistent with seismic observations. It is found that the analytical predictions from KdV model fit better with seismic and satellite observations than the eKdV model in this case without consideration of the background currents. The waveshapes and kinematic characteristics presented here suggest that not all the solitons originate from the same source and the ISW train maybe composed of several subgroups.

#### Acknowledgments

We thank the captain, crew, and science party of R/V SHIYAN2 for acquiring the seismic data and XBT data. Both are available for academic research at website <http://pan.baidu.com/s/1c0wI52k>. Anonymous reviewers are greatly acknowledged for their constructive comments and suggestions. The Tide Model Driver (TMD) software was used for tidal prediction. This research was supported financially by the NSFC (grants 41376023 and 41176026) and the ZPNSFC (LQ12D06003). This work was also partially supported by Chinese Scholarship Council (201408440021) for a visit by Q.T. to Durham University.

#### References

- Apel, J. R., L. A. Ostrovsky, Y. A. Stepanyants, and J. F. Lynch (2007), Internal solitons in the ocean and their effect on underwater sound, *J. Acoust. Soc. Am.*, *121*(2), 695–722, doi:10.1121/1.2395914.
- Ballabrera-Poy, J., B. Mourre, E. Garcia-Ladona, A. Turiel, and J. Font (2009), Linear and non-linear T-S models for the eastern North Atlantic from Argo data: Role of surface salinity observations, *Deep Sea Res., Part I*, *56*(10), 1605–1614, doi:10.1016/j.dsr.2009.05.017.
- Biescas, B., V. Sallares, J. L. Pelegri, F. Machin, R. Carbonell, G. Buffett, J. J. Danobeitia, and A. Calahorrano (2008), Imaging meddy finestructure using multichannel seismic reflection data, *Geophys. Res. Lett.*, *35*, L11609, doi:10.1029/2008GL033971.
- Biescas, B., L. Armi, V. Sallares, and E. Gracia (2010), Seismic imaging of staircase layers below the Mediterranean Undercurrent, *Deep Sea Res., Part I*, *57*(10), 1345–1353, doi:10.1016/j.dsr.2010.07.001.
- Biescas, B., B. R. Ruddick, M. R. Nedimovic, V. Sallares, G. Bornstein, and J. F. Mojica (2014), Recovery of temperature, salinity, and potential density from ocean reflectivity, *J. Geophys. Res. Oceans*, *119*, 3171–3184, doi:10.1002/2013JC009662.
- Buffett, G. G., R. W. Hobbs, E. A. Vsemirnova, D. Klaeschen, C. A. Hurich, C. Ranero, and V. Sallarès (2013), Characterization of thermohaline staircases in the Tyrrhenian sea using stochastic heterogeneity mapping, *J. Acoust. Soc. Am.*, *133*, 3313, doi:10.1121/1.4805513.
- Buijsman, M. C., Y. Kanarska, and J. C. McWilliams (2010), On the generation and evolution of nonlinear internal waves in the South China Sea, *J. Geophys. Res.*, *115*, C02012, doi:10.1029/2009JC005275.
- Cai, S., J. Xie, and J. He (2012), An overview of internal solitary waves in the South China Sea, *Surv. Geophys.*, *33*(5), 927–943, doi:10.1007/s10712-012-9176-0.
- Cai, S. Q., X. M. Long, and Z. J. Gan (2002), A numerical study of the generation and propagation of internal solitary waves in the Luzon Strait, *Oceanol. Acta*, *25*(2), 51–60.
- Cai, S. Q., S. G. Wang, and X. M. Long (2006), A simple estimation of the force exerted by internal solitons on cylindrical piles, *Ocean Eng.*, *33*(7), 974–980, doi:10.1016/j.oceaneng.2005.05.012.
- Carniel, S., A. Bergamasco, J. W. Book, R. W. Hobbs, M. Sclavo, and W. T. Wood (2012), Tracking bottom waters in the Southern Adriatic Sea applying seismic oceanography techniques, *Cont. Shelf Res.*, *44*, 30–38.
- Chang, M. H., R. C. Lien, Y. J. Yang, and T. Y. Tang (2011), Nonlinear internal wave properties estimated with moored ADCP measurements, *J. Atmos. Oceanic Technol.*, *28*(6), 802–815, doi:10.1175/2010jtecho814.1.
- Du, T., Y. H. Tseng, and X. H. Yan (2008), Impacts of tidal currents and Kuroshio intrusion on the generation of nonlinear internal waves in Luzon Strait, *J. Geophys. Res.*, *113*, C08015, doi:10.1029/2007JC004294.
- Faraway, J. J. (1998), Data splitting strategies for reducing the effect of model selection on inference, *Comput. Sci. Stat.*, *30*, 332–341.
- Farmer, D., and L. Armi (1999), The generation and trapping of solitary waves over topography, *Science*, *283*(5399), 188–190, doi:10.1126/science.283.5399.188.
- Farmer, D., Q. Li, and J. H. Park (2009), Internal wave observations in the South China Sea: The role of rotation and non-linearity, *Atmos. Ocean*, *47*(4), 267–280, doi:10.3137/Oc313.2009.
- Fer, I., P. Nandi, W. S. Holbrook, R. W. Schmitt, and P. Paramo (2010), Seismic imaging of a thermohaline staircase in the western tropical North Atlantic, *Ocean Sci.*, *6*(3), 621–631, doi:10.5194/os-6-621-2010.
- Fliegel, M., and K. Hunkins (1975), Internal wave dispersion calculated using Thomson-Haskell method, *J. Phys. Oceanogr.*, *5*(3), 541–548.
- Gonella, J., and D. Michon (1988), Ondes internes profondes révélées par sismique réflexion au sein des masses d'eau en Atlantique-Est = Deep internal waves measured by seismic-reflection within the eastern Atlantic water mass, *Multilingue*, *306*(12), 781–787.
- Grimshaw, R., E. Pelinovsky, and O. Poloukhina (2002), Higher-order Korteweg-de Vries models for internal solitary waves in a stratified shear flow with a free surface, *Nonlinear Processes Geophys.*, *9*(3–4), 221–235.
- Grimshaw, R., E. Pelinovsky, T. Talipova, and O. Kurkina (2010), Internal solitary waves: Propagation, deformation and disintegration, *Nonlinear Processes Geophys.*, *17*(6), 633–649.
- Grue, J., A. Jensen, P.-O. Rusas, and J. Svein (1999), Properties of large-amplitude internal waves, *J. Fluid Mech.*, *380*, 257–278.
- Gumley, L., J. Desclotres, and J. Schmaltz (2010), *Creating Reprojected True Color Modis Images: A Tutorial*, Univ. of Wis., Madison.
- Guo, C., and X. Chen (2014), A review of internal solitary wave dynamics in the northern South China Sea, *Prog. Oceanogr.*, *121*, 7–23, doi:10.1016/j.poccean.2013.04.002.
- Helfrich, K. R., and W. K. Melville (2006), Long nonlinear internal waves, *Annu. Rev. Fluid Mech.*, *38*, 395–425.
- Holbrook, W. S., P. Paramo, S. Pearce, and R. W. Schmitt (2003), Thermohaline fine structure in an oceanographic front from seismic reflection profiling, *Science*, *301*(5634), 821–824.
- Holbrook, W. S., I. Fe, R. W. Schmitt, D. Lizarralde, J. M. Klymak, L. C. Helfrich, and R. Kubickek (2013), Estimating oceanic turbulence dissipation from seismic images, *J. Atmos. Oceanic Technol.*, *30*, 1767–1788, doi:10.1175/JTECH-D-12-00140.1.
- Jackson, C. R. (2009), An empirical model for estimating the geographic location of nonlinear internal solitary waves, *J. Atmos. Oceanic Technol.*, *26*(10), 2243–2255, doi:10.1175/2009jtecho638.1.

- Jones, I. F., and S. Levy (1987), Signal-to-noise ratio enhancement in multichannel seismic data via the Karhunen-Loeve transform, *Geophys. Prospect.*, *35*(1), 12–32, doi:10.1111/j.1365-2478.1987.tb00800.x.
- Klaeschen, D., R. W. Hobbs, G. Krahnemann, C. Papenberg, and E. Vsemirnova (2009), Estimating movement of reflectors in the water column using seismic oceanography, *Geophys. Res. Lett.*, *36*, L00D03, doi:10.1029/2009GL038973.
- Klymak, J. M., and M. C. Gregg (2004), Tidally generated turbulence over the Knight Inlet sill, *J. Phys. Oceanogr.*, *34*(5), 1135–1151.
- Kormann, J., B. Biescas, N. Korta, J. de la Puente, and V. Sallares (2011), Application of acoustic full waveform inversion to retrieve high-resolution temperature and salinity profiles from synthetic seismic data, *J. Geophys. Res.*, *116*, C11039, doi:10.1029/2011JC007216.
- Li, X. F., C. R. Jackson, and W. G. Pichel (2013), Internal solitary wave refraction at Dongsha Atoll, South China Sea, *Geophys. Res. Lett.*, *40*, 3128–3132, doi:10.1002/grl.50614.
- Liu, A. K., Y. S. Chang, M. K. Hsu, and N. K. Liang (1998), Evolution of nonlinear internal waves in the East and South China Seas, *J. Geophys. Res.*, *103*(C4), 7995–8008.
- Michallet, H., and E. Barthelemy (1998), Experimental study of interfacial solitary waves, *J. Fluid Mech.*, *366*, 159–177.
- Nakamura, Y., T. Noguchi, T. Tsuji, S. Itoh, H. Niino, and T. Matsuoka (2006), Simultaneous seismic reflection and physical oceanographic observations of oceanic fine structure in the Kuroshio extension front, *Geophys. Res. Lett.*, *33*, L23605, doi:10.1029/2006GL027437.
- Orr, M. H., and P. C. Mignerey (2003), Nonlinear internal waves in the South China Sea: Observation of the conversion of depression internal waves to elevation internal waves, *J. Geophys. Res.*, *108*(C3), 3064, doi:10.1029/2001JC001163.
- Pelinovskii, E. N., O. E. Polukhina, and K. Lamb (2000), Nonlinear internal waves in the ocean stratified in density and current, *Oceanology*, *40*(6), 757–766.
- Phillips, J. D., and D. F. Dean (1991), Multichannel Acoustic Reflection Profiling of Ocean Watermass Temperature/Salinity Interfaces, in *Ocean Variability & Acoustic Propagation*, edited by J. Poner and A. Warn-Vamos, pp. 199–214, Springer, N. Y.
- Piété, H., L. Marié, B. Marsset, Y. Thomas, and M.-A. Gutscher (2013), Seismic reflection imaging of shallow oceanographic structures, *J. Geophys. Res. Oceans*, *118*, 2329–2344, doi:10.1002/jgrc.20156.
- Pinheiro, L. M., H. B. Song, B. Ruddick, J. Dubert, I. Ambar, K. Mustafa, and R. Bezerra (2010), Detailed 2-D imaging of the Mediterranean outflow and meddies off W Iberia from multichannel seismic data, *J. Mar. Syst.*, *79*(1–2), 89–100, doi:10.1016/j.jmarsys.2009.07.004.
- Ramp, S. R., T. Y. Tang, T. F. Duda, J. F. Lynch, A. K. Liu, C. S. Chiu, F. L. Bahr, H. R. Kim, and Y. J. Yang (2004), Internal solitons in the northeastern South China Sea - Part I: Sources and deep water propagation, *IEEE J. Oceanic Eng.*, *29*(4), 1157–1181, doi:10.1109/JOE.2004.840839.
- Ramp, S. R., Y. J. Yang, and F. L. Bahr (2010), Characterizing the nonlinear internal wave climate in the northeastern South China Sea, *Nonlinear Processes Geophys.*, *17*(5), 481–498, doi:10.5194/npg-17-481-2010.
- Reeder, D. B., B. B. Ma, and Y. J. Yang (2011), Very large subaqueous sand dunes on the upper continental slope in the South China Sea generated by episodic, shoaling deep-water internal solitary waves, *Mar. Geol.*, *279*(1–4), 12–18, doi:10.1016/j.margeo.2010.10.009.
- Sheen, K. L., N. White, C. P. Caulfield, and R. W. Hobbs (2011), Estimating geostrophic shear from seismic images of oceanic structure, *J. Atmos. Oceanic Technol.*, *28*(9), 1149–1154, doi:10.1175/Jtech-D-10-05012.1.
- Sheen, K. L., N. J. White, C. P. Caulfield, and R. W. Hobbs (2012), Seismic imaging of a large horizontal vortex at abyssal depths beneath the Sub-Antarctic Front, *Nat. Geosci.*, *5*(8), 542–546, doi:10.1038/Ngeo1502.
- Tang, Q. S., D. X. Wang, J. B. Li, P. Yan, and J. Li (2013), Image of a subsurface current core in the southern South China Sea, *Ocean Sci.*, *9*(4), 631–638, doi:10.5194/os-9-631-2013.
- Tang, Q. S., S. P. S. Gulick, and L. T. Sun (2014a), Seismic observations from a Yakutat eddy in the northern Gulf of Alaska, *J. Geophys. Res. Oceans*, *119*, 3535–3547, doi:10.1002/2014JC009938.
- Tang, Q. S., C. X. Wang, D. X. Wang, and R. Pawlowicz (2014b), Seismic, satellite, and site observations of internal solitary waves in the NE South China Sea, *Sci. Rep.*, *4*, 5374, doi:10.1038/srep05374.
- Teague, W. J., H. W. Wijesekera, W. E. Avera, and Z. R. Hallock (2011), Current and density observations of packets of nonlinear internal waves on the outer New Jersey Shelf, *J. Phys. Oceanogr.*, *41*(5), 994–1008, doi:10.1175/2010jpo4556.1.
- Trevorrow, M. V. (1998), Observations of internal solitary waves near the Oregon coast with an inverted echo sounder, *J. Geophys. Res.*, *103*(C4), 7671–7680.
- Vlasenko, V., C. Guo, and N. Stashchuk (2012), On the mechanism of A-type and B-type internal solitary wave generation in the northern South China Sea, *Deep Sea Res., Part I*, *69*, 100–112, doi:10.1016/j.dsr.2012.07.004.
- Vsemirnova, E., R. Hobbs, N. Serra, D. Klaeschen, and E. Quentel (2009), Estimating internal wave spectra using constrained models of the dynamic ocean, *Geophys. Res. Lett.*, *36*, L00D07, doi:10.1029/2009GL039598.
- Wang, C., and R. Pawlowicz (2011), Propagation speeds of strongly nonlinear near-surface internal waves in the Strait of Georgia, *J. Geophys. Res.*, *116*, C10021, doi:10.1029/2010JC006776.
- Yuan, Y. L., Q. N. Zheng, D. J. Dai, X. M. Hu, F. L. Qiao, and J. M. Meng (2006), Mechanism of internal waves in the Luzon Strait, *J. Geophys. Res.*, *111*, C11S17, doi:10.1029/2005JC003198.
- Zhang, P., S. Tang, K. Qu, and Q. Zhang (2012), Test and analysis on domestic-made XBT probe, *Tech. Acoust.*, *31*(6), 570–573.
- Zhao, W., X. D. Huang, and J. W. Tian (2012), A new method to estimate phase speed and vertical velocity of internal solitary waves in the South China Sea, *J. Oceanogr.*, *68*(5), 761–769, doi:10.1007/s10872-012-0132-x.
- Zhao, Z. X., and M. H. Alford (2006), Source and propagation of internal solitary waves in the northeastern South China Sea, *J. Geophys. Res.*, *111*, C11012, doi:10.1029/2006JC003644.
- Zhao, Z. X., V. Klemas, Q. N. Zheng, and X. H. Yan (2004), Remote sensing evidence for baroclinic tide origin of internal solitary waves in the northeastern South China Sea, *Geophys. Res. Lett.*, *31*, L06302, doi:10.1029/2003GL019077.
- Zheng, Q., R. D. Susanto, C. R. Ho, Y. T. Song, and Q. Xu (2007), Statistical and dynamical analyses of generation mechanisms of solitary internal waves in the northern South China Sea, *J. Geophys. Res.*, *112*, C03021, doi:10.1029/2006JC003551.